



Minerva Access is the Institutional Repository of The University of Melbourne

Author/s:

Liao, JJ;Smith, DW;Miramini, S;Thibbotuwawa, N;Gardiner, BS;Zhang, L

Title:

The investigation of fluid flow in cartilage contact gap

Date:

2019-07-01

Citation:

Liao, J. J., Smith, D. W., Miramini, S., Thibbotuwawa, N., Gardiner, B. S. & Zhang, L. (2019). The investigation of fluid flow in cartilage contact gap. *Journal of the Mechanical Behavior of Biomedical Materials*, 95, pp.153-164. <https://doi.org/10.1016/j.jmbbm.2019.04.008>.

Persistent Link:

<https://hdl.handle.net/11343/245473>

THE INVESTIGATION OF FLUID FLOW IN CARTILAGE

CONTACT GAP

JinJing Liao^a, David W. Smith^b, Saeed Miramini^a, Namal Thibbotuwawa^d, Bruce S. Gardiner^c, Lihai Zhang^{a*}

^a Department of Infrastructure Engineering, The University of Melbourne, Victoria 3010, Australia

^b Faculty of Engineering, Computing and Mathematics, The University of Western Australia, WA 6009, Australia

^c School of Engineering and Information Technology, Murdoch University, WA 6150, Australia

^d School of Chemistry, Physics and Mechanical Engineering, Queensland University of Technology, QLD 4001, Australia

* Corresponding author (Email: lihzhang@unimelb.edu.au)

Highlights:

- Study fluid flow in cartilage gap by developing validated numerical models.
- Synthesise cartilage topography using the measurements from Dektak Stylus Profilers.
- Contact gap height and fluid pressure gradient greatly affect the gap permeability.
- The gap is functionally closed at particular gap height and pressure gradient.

26 **Abstract.** *Synovial fluid flow in articular joint capsule plays an important role during*
27 *mixed mode lubrication.* However, the actual fluid flow behaviour during cartilage
28 contact has not been fully understood so far. This is due to the difficulties in
29 measuring the gap permeability using conventional experimental techniques. The
30 problem becomes further complicated with consideration of the cartilage surface
31 roughness. Here a validated numerical study was developed to quantify the gap
32 permeability to lateral synovial fluid flow. Both macro and micro scale gap flow
33 models were created based on Darcy's law at the macroscale and the Navier-
34 stokes equation at the microscale. To generate model inputs, the cartilage
35 topography was numerically synthesised based on the experimental measurements
36 of bovine media tibia cartilage using Dektak Stylus Profilers. The experimental
37 results show that the average surface roughness R_a is $1.97 \mu\text{m}$ and root-mean-square
38 roughness R_q is $2.44 \mu\text{m}$, while the correlation lengths of the secondary and tertiary
39 undulations are round $100 \mu\text{m}$ and $20 \mu\text{m}$, respectively. The numerical results indicate
40 that the contact gap height and fluid pressure gradient are two critical parameters
41 which significantly affect the gap permeability. As the contact gap closes, there is
42 a decrease in gap permeability, and most importantly, the gap permeability is also
43 very sensitive to the fluid pressure gradient. Furthermore, with gap closure, the
44 permeability of the contact gap gradually approaches that of the cartilage tissue, at
45 which point the contact gap is functional closed. This occurs at a contact gap
46 around $1 \mu\text{m}$ and for a fluid pressure gradient is below $5 \times 10^5 \text{ Pa/m}$.

47 **Keywords:** cartilage; contact gap; gap permeability; surface roughness; synovial fluid.

48

49 1 INTRODUCTION

50 Man-made contacts (e.g. bearings) are designed to be smooth for achieving a low
51 friction (and wear) surface. Animal joint bearings have developed their own solution.
52 Within articulating joints, the porous cartilage surface is relatively rough (see Fig.1),
53 but despite the surface roughness, cartilage's initial friction coefficient of ~ 0.01
54 outperforms any current man-made bearings (Merkher et al., 2006).

55 Cartilage lubrication and/or frictional properties has been previously organised
56 by stages of contact between two opposing surfaces, namely hydrodynamic
57 lubrication, mixed lubrication and boundary lubrication (Neu et al., 2008). **Mixed
58 mode lubrication which is a state involving hydrodynamic lubrication, boundary
59 lubrication and biphasic lubrication by interstitial fluid pressurisation is responsible for
60 the low friction and wear of cartilage (Ateshian, 2009).**

61 The concept of "weeping lubrication" was first proposed by McCutchen (1959).
62 According to this theory (McCutchen, 1962), the compression of asperities in the
63 contact gap pressurises interstitial fluid within the cartilage, and the interstitial fluid
64 then flows down its pressure gradient to "weep" into the contact gap. With the
65 pressurised incompressible fluid in the contact gap initially carrying most of the
66 applied load, the friction is reduced significantly. This hydrodynamic lubrication
67 mechanism is significantly extended in time due to the fluid lost from the contact
68 gap being replenished by fluid that "weeps" into the contact gap from the cartilage.
69 On the other hand, the boosted lubrication theory was proposed by Walker et al.
70 (1968, 1969), which argued that the pressurised synovial fluid is more likely to
71 undergo ultrafiltration, the gap fluid flowing down its pressure gradient into the
72 cartilage, leaving behind a concentrated protein gel that acted as a boundary
73 lubricant.

74 In the last decades, significant progress has been made in the understanding of
75 biotribology of cartilage. Biphasic lubrication that emphasises on the load support
76 capability of the pressurised interstitial fluid inside cartilages rather than the
77 lubricants in the gap have been proposed (Ateashian, 2009). It is argued that the
78 high-level interstitial fluid pressurisation inside the cartilage could minimise direct
79 solid phase shear between the contact surfaces and hence reduce the friction.
80 Recently, the replenishment of interstitial fluid from imbibition during joint cartilage
81 swell (“tribological rehydration”) has been reported by Moore and Burris (2017).
82 Through multiple start-stop cartilage-on-glass sliding tests, they concluded that the
83 interstitial fluid lost in static loading could be recovered during sliding because the
84 hydrodynamic pressure pushed the fluid in the contact gap into cartilage tissue,
85 and the resultant flow into the tissue enhanced solute transport (Graham et al.,
86 2017).

87 As per the short review above, the fluid flow in the contact gap plays an important
88 role in cartilage mixed mode contact, and hence a better understanding on the fluid
89 flow behaviour in the contact gap is essential. As shown in Fig.1, there are two
90 potential fluid paths from the contact gap, one is through fluid exchange with the
91 cartilage, the other is lateral outflow across the perimeter of the contact gap. The
92 dominance of one path over the other is likely to vary throughout the time course
93 of the contact. Indeed, given the time-dependent poroelastic properties of cartilage,
94 the flow paths and cartilage’s frictional properties are expected to change (Zhang
95 et al., 2015). Wu and Ferguson (2017) have laid a foundation on this issue by
96 studying the effects of asperity distribution, root-mean-square (RMS) roughness,
97 wavelengths and flow angle on the contact gap permeability. However as discussed
98 later, in Wu and Ferguson (2017)’s analysis the synovial fluid is assumed to be

99 Newtonian viscosity, while the randomness of surface roughness is not guaranteed
100 statistically (i.e., sample dimensions and sizes were not large enough, the
101 wavelengths were not random).

102 Since no contact model has addressed the interaction between the gap flow with
103 non-Newtonian properties (Mow et al., 1993). This study represents a first step
104 towards understanding the fundamental fluid flow behaviour in the contact gap. This
105 understanding is essential not only for understanding synovial joint behaviour, but
106 also for the development of bio-inspired smart materials (Greene et al., 2014),
107 which have a variety of practical applications in the fields of daily life, industry, and
108 agriculture (e.g. cartilage-inspired lubrication system). We first measured the
109 surface roughness by using bovine cartilage, and then the synthetic surfaces of
110 cartilage were developed by employing an advanced mathematical algorithm with
111 key measured parameters (i.e., average roughness R_a , RMS roughness R_q and
112 correlation length). The methodology allows for multiple sample investigations to
113 satisfy statistical requirements with less computational cost. A micro-scale of
114 computational fluid dynamics (CFD) model with non-Newtonian viscosity was
115 employed to investigate the fluid flow in contact gap between two cartilages. Finally,
116 the gap permeability can be estimated by the gap height and fluid pressure gradient.

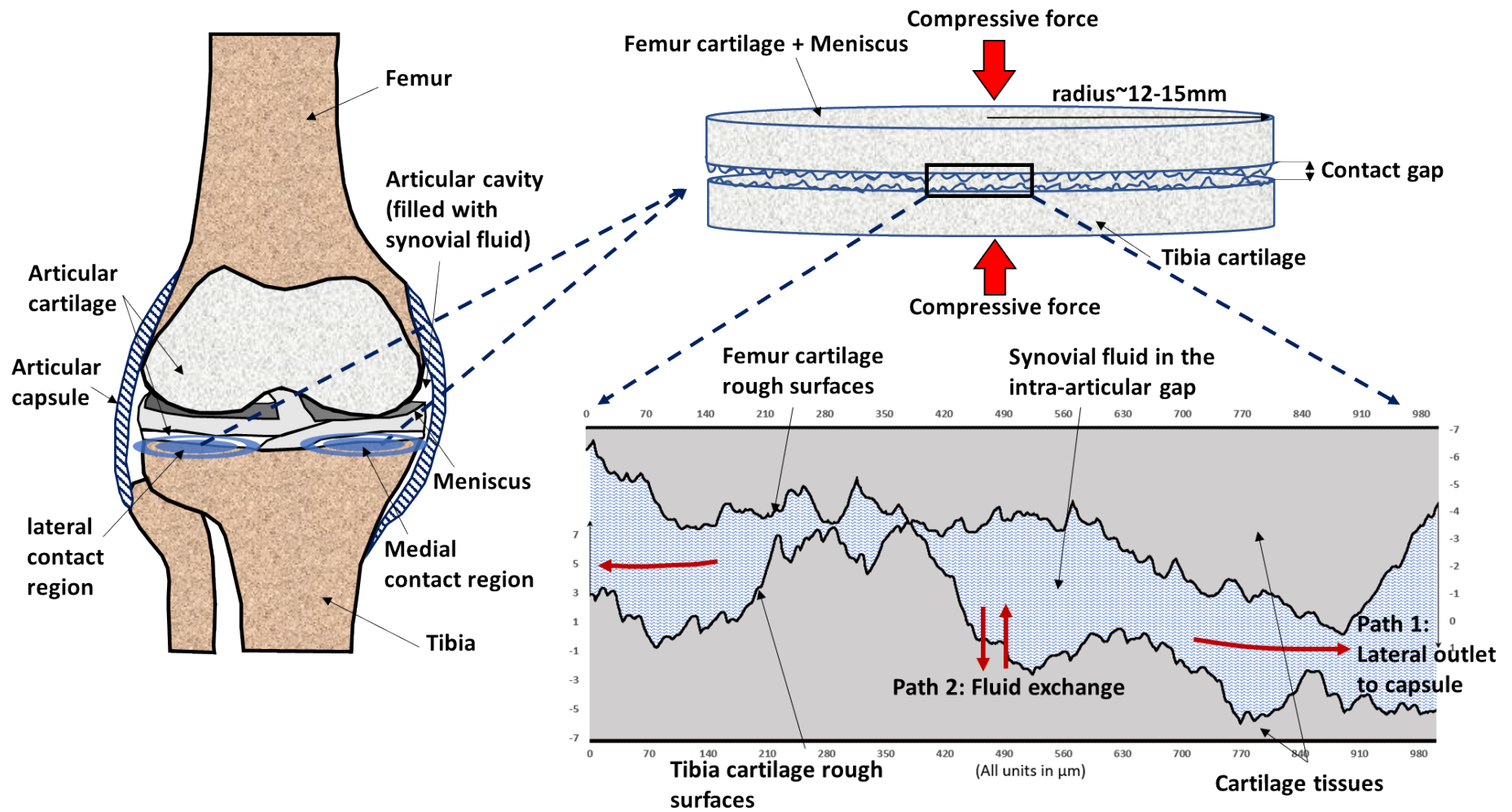


Fig.1 –Schematic diagram showing fluid flow in cartilage contact gap.

117

118

119 2 MATERIALS AND METHODS

120 2.1 Methods

121 The physical configuration of the problem is a simplification of the synovial knee
122 joint (see Fig.1). By treating the femur and meniscus as one body, we can obtain two
123 approximately circular contact regions between femur-meniscus and tibia (lateral and
124 medial), with a radius of 12-15 mm each (Marzo and Gurske-DePerio, 2009).
125 Furthermore, by ignoring the femur head curvature, the problem can be simplified as
126 two cylindrical cartilage discs. The above simplifications have often been used when
127 investigating the squeeze film behaviour of joint lubrication (Bujurke and Kudenatti,
128 2006), in which a thick fluid film separates two cartilages. On initial contact of cartilage
129 surface asperities, the joint lubrication mode shifts from squeeze film to mixed mode
130 lubrication. This general account of gap behaviour is elementary: it simply says that
131 initially the two contacting surface are (potentially) separated by fluid, and then they
132 contact at asperities, establishing simultaneous boundary lubrication and
133 hydrodynamic lubrication, which is referred to as mixed mode lubrication. Based on
134 the measurements in this study, the initial cartilage surface roughness is randomly
135 distributed. A schematic depiction of the inferred cross-section profiles (based on
136 measurement data of the initial profiles) of femur and tibia some time after initial under
137 contact is shown in Fig.1. With the heights and uneven contact of the randomly
138 distributed asperities, there will form an interconnected pore space that is described
139 here as the “contact gap”. For a single load event such as standing up for some time,
140 the two cartilage discs can be assumed under quasi-static compression, which will
141 cause the contact gap closure and thereby change the fluid behaviour in the gap.

142 This study primarily focuses on the fluid flow in/out cartilage contact gap (Path
143 1, Fig.1), so that the simulations are initiated when highest asperities of two

144 cartilage surfaces are about to (or just in) contact. The fluid permeability under
145 different gap heights (simulation of gap closure) is estimated by applying pressure
146 difference at the two ends of contact gap (Fig.2). To simplify the complicated fluid
147 flow behaviour in the contact gap, the following assumptions are made in this study:

- 148 • The contact surface topography of two the cartilage surfaces are assumed
149 to be symmetrical during contact. This assumption can greatly simplify the
150 contact geometry without sacrificing the fundamental fluid flow behaviour in
151 the contact gap.
- 152 • The fluid exchange between contact gap and cartilage tissue, and the bulk
153 deformation of cartilage tissue are not considered in the study. This is
154 because the gap permeability is related to the pore space in the contact gap,
155 and the closing of the contact gap is primarily dependent on the asperity
156 level deformation.
- 157 • Fluid-structure interaction in cartilage contact gap is not considered because
158 it is not the primary focus of this study and its effect is probably minor. This is
159 because solid matrices of asperities are incompressible, and in a pressure
160 continuum space, the interstitial fluid pressure inside the asperity tissues
161 tends to cancel out some of the outside fluid pressure in the contact gap.
162 Therefore, the asperity deformation caused by fluid pressure in the gap is
163 minimal compared to the external loading.
- 164 • The fluid flow in macro and micro scales can be modelled by Darcy's law
165 and Navier-Stokes equation, respectively.

166 At the macro-scale, the contact gap between asperities of two cartilages forms
167 interconnected pore spaces, and the gap flow behaviour can be described by
168 Darcy's law in cylindrical coordinates,

$$169 \quad \mathbf{v}_d = -\frac{\kappa}{\mu} \nabla p = -K_r \frac{\Delta p}{\Delta r} \quad (1)$$

170 where K_r is the gap permeability, which represents the degree of difficulty for the
171 flow to exit laterally. \mathbf{v}_d is the Darcy velocity of the gap flow. p is the pressure of the
172 fluid in the gap generated by the external load. μ is the viscosity of the synovial
173 fluid. κ is the intrinsic permeability of the gap which is primarily dependent on the
174 geometry of the pores in the gap, and in turn is function of the distribution of asperity
175 size and gap height h (i.e., $\kappa = \kappa(h)$). Since the centre line (mean) of the cartilage
176 rough surface is usually taken at $z = 0$, the gap height h is defined as the distance
177 between the centre lines of the upper and lower cartilage, which is also twice of the
178 distance between the symmetrical line and the centre line of cartilage roughness in
179 this study (Fig.2). Therefore, the gap height h covers the positive asperity heights
180 (peaks) of the upper and lower cartilage rough surface.

181 To guarantee statistical randomness, the selection of representative elementary
182 volume (REV) for the micro-scale model is vital. In porous media, the REV is
183 determined by gradually enlarging the averaging sample size to achieve relatively
184 constant readings for variables (Bear, 1988). It is discovered that over a length
185 scale of 250 μm the asperities are relatively high and the peak heights are
186 measured in around 10 μm . The maximum peak heights measured from square
187 bovine knee joint samples of 250 μm in length ranged from 6-18 μm (Graindorge et
188 al., 2006). The levelled equine joint samples taken from three joint types (radiocarpal,
189 midcarpal and carpometacarpal) with a length scale of 5000 μm scanned by Smyth et

190 al. (2012) showed that the asperity heights were around 5-10 μm . This finding is
 191 consistent with the experimental measurements carried out in this study (R_p value in
 192 Table 1 is close to 10 μm), which is based on a 1000 $\mu\text{m} \times 1000 \mu\text{m}$ sample size. These
 193 findings imply that, at a contact length over 250 μm , the maximum gap size between
 194 two contact cartilages is around 20 μm . Therefore, in the present study a REV of 1000
 195 $\mu\text{m} \times 1000 \mu\text{m}$ is considered as the suitable size for the cartilage contact problem. On
 196 the other hand, if we assume two primary roughly circular contact regions (lateral and
 197 media, each with a radius of 12-15 mm, see Fig.1) are generated during standing or
 198 walking, the size of each contact area in the knee is around 500-700 mm^2 (based on
 199 the contact radius of 12-15 mm), compared to which the area of the REV is 1/700-
 200 1/500. This implies the chosen REV size is appropriate to the scale for the *in vivo* knee
 201 cartilage contact problem.

202 Isothermal, laminar, incompressible flow conditions are assumed in the gap for the
 203 micro-scale REV model (1 mm \times 1 mm square). The flow is governed by the Navier-
 204 Stokes equations in Cartesian coordinates.

$$205 \quad \begin{cases} \nabla \cdot \mathbf{u} = 0 \\ \rho \frac{\partial \mathbf{u}}{\partial t} + \rho(\mathbf{u} \cdot \nabla) \mathbf{u} = \nabla \cdot [-p\mathbf{I} + \mu(\dot{\boldsymbol{\gamma}}) \cdot \dot{\boldsymbol{\gamma}}] + \mathbf{F} \end{cases} \quad (2)$$

206 where ρ is the density of synovial fluid; \mathbf{u} is fluid velocity vector; p is fluid pressure;
 207 \mathbf{F} is the volume force vector which is ignored in this study; μ is the viscosity of
 208 synovial fluid. $\dot{\boldsymbol{\gamma}}$ is the shear rate tensor, its expression and its magnitude shear
 209 rate $\dot{\gamma}$ are given below,

$$210 \quad \begin{aligned} \dot{\boldsymbol{\gamma}} &= \nabla \mathbf{u} + (\nabla \mathbf{u})^T; \\ \dot{\gamma} &= |\dot{\boldsymbol{\gamma}}| = \sqrt{\frac{1}{2} \dot{\boldsymbol{\gamma}} : \dot{\boldsymbol{\gamma}}} \end{aligned} \quad (3)$$

211 Recent studies of the synovial fluid flow in the contact gap mainly treated
212 synovial fluid as a Newtonian fluid with constant viscosity (e.g. 1 Pa·s was used by
213 Wu and Ferguson, 2017, and 0.6 Pa·s by Moghadam et al., 2014). However,
214 synovial fluid is a non-Newtonian fluid with a shear-thinning effect, i.e., the viscosity
215 decreases with increasing shear rate (Fam et al., 2007). The relationship between
216 viscosity and shear rate is usually obtained from viscometer experiments on
217 oscillating flow, in which the synovial fluid is pre-sheared for two minutes, and then
218 different shear rates are applied to the sample until the steady state is reached
219 (Bhuanantanondh, 2009). Initially, the viscosity of synovial fluid is high due to the
220 randomly orientated long molecules, then it decreases as the long molecules are
221 re-orientated and stretched in the direction of the flow lines. In this study, the
222 viscosity of synovial fluid is defined by gap height and fluid velocity (i.e., $\mu = \mu(h,u)$)
223 through relating the shear rate to the gap height and fluid velocity as per Eq. (3). In
224 addition, synovial fluid also exhibits time dependent shear thickening. To remove time-
225 dependent synovial fluid behaviour, this study mainly focused on the long-term steady
226 state conditions, under which conditions synovial fluid can be reasonably modelled as
227 a shear thinning fluid.

228 In order to better capture the gap flow behaviour, two major inputs are
229 incorporated in the micro-scale REV model.

- 230 1. Experimentally measured and numerically synthesised cartilage surface
231 roughness.
- 232 2. Constitutive relationship for synovial fluid by curve-fitting the experimental
233 data of steady state oscillating flow.

234 The link from the micro to macro scale is drawn by equating the volume-
235 averaged velocity of the REV (microscale) to the Darcy velocity in macro scale.
236 Thus, the macro scale gap permeability K_r can be evaluated.

$$\begin{aligned} u_{vol.ave} &= \frac{1}{V} \int_{REV} u_i \cdot dV_i = v_d \\ K_r &= v_d \frac{\Delta r}{\Delta p} = u_{vol.ave} \frac{\Delta r}{\Delta p} \end{aligned} \quad (4)$$

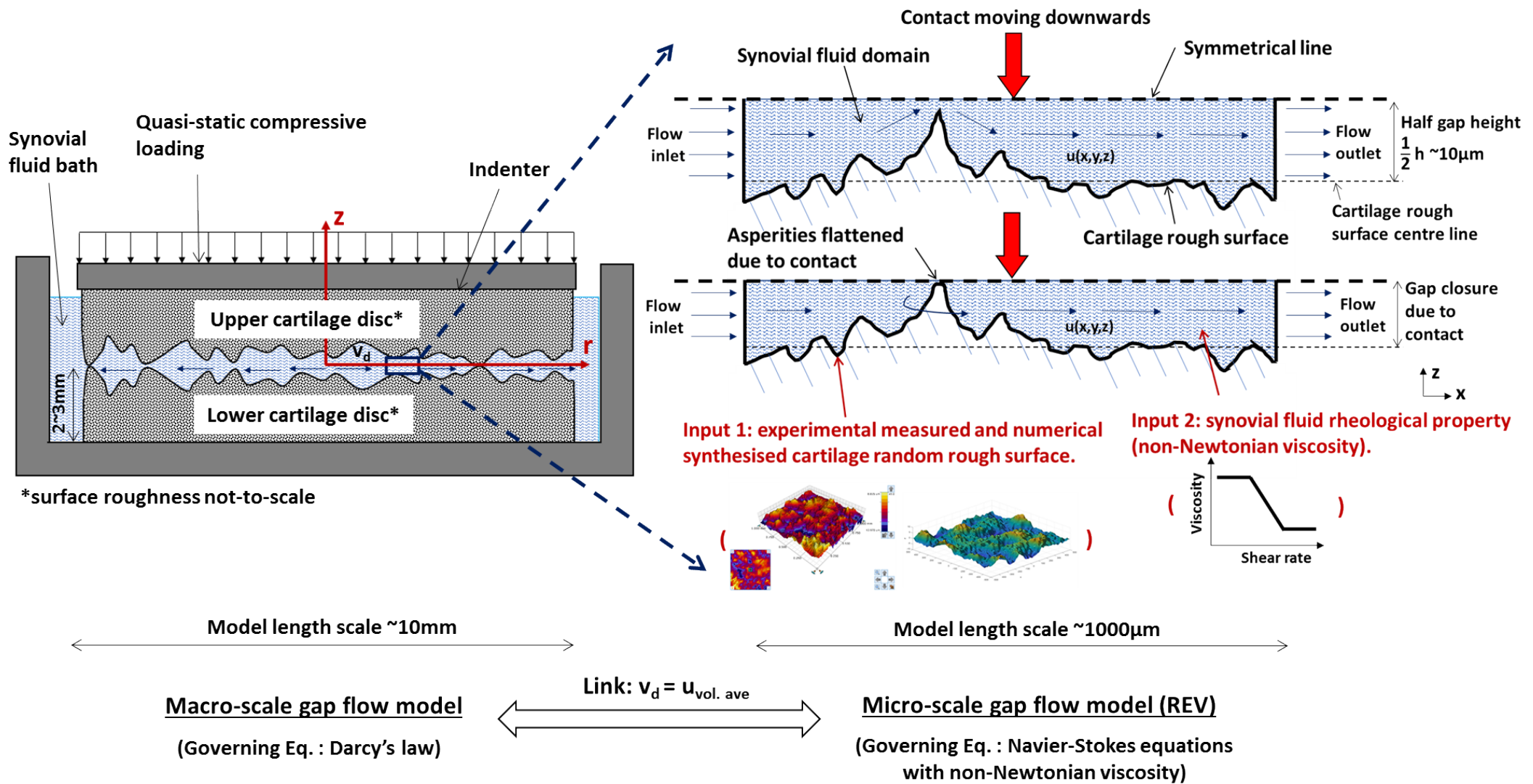


Fig.2 – An overview of the proposed numerical approach.

238

239

240 **2.2 Reconstruction of cartilage surface topography**

241 **2.2.1 Experimental measurements of cartilage surface roughness**

242 Bovine patellofemoral joints ($n = 3$) of 2 to 4-year-old animals were sourced from
243 abattoir and were dissected to obtain fresh tibias with microscopically normal cartilage.
244 The femurs were soaked in 0.15M Phosphate-buffered saline solution and stored at
245 minus 20 degrees C.

246 Prior to harvesting the osteochondral sample blocks (approximately 1 cm × 1 cm)
247 from lateral femur, the intact femur was thawed in 0.15M Phosphate-buffered saline
248 at room temperature. The osteochondral blocks were then glued (LOCTITE® SUPER
249 GLUE GEL CONTROL™) on a glass slide (Fig.3 (b)) and were loaded on to the stage
250 of a stylus profiler (DektakXT, Bruker) (Fig.3 (a)) for the roughness measurements.

251 Surface scanning was conducted using a 2 μm tip over an area of 1 mm × 1 mm,
252 approximately at the middle of the sample. Stylus force of 1 mg was used for the
253 scanning and samples were kept hydrated throughout. The scanning speed was set
254 to 100 μm/s with a Y-resolution of 0.33 μm/pt, 200 scans in the X-direction and vertical
255 resolution (Z-resolution) of 8nm (Fig.3 (c)). Each sample took approximately 40 mins
256 to scan and the 3D scanned profiles were analysed using DektakXT inbuilt
257 Vision64 software to obtain the roughness parameters of the cartilage

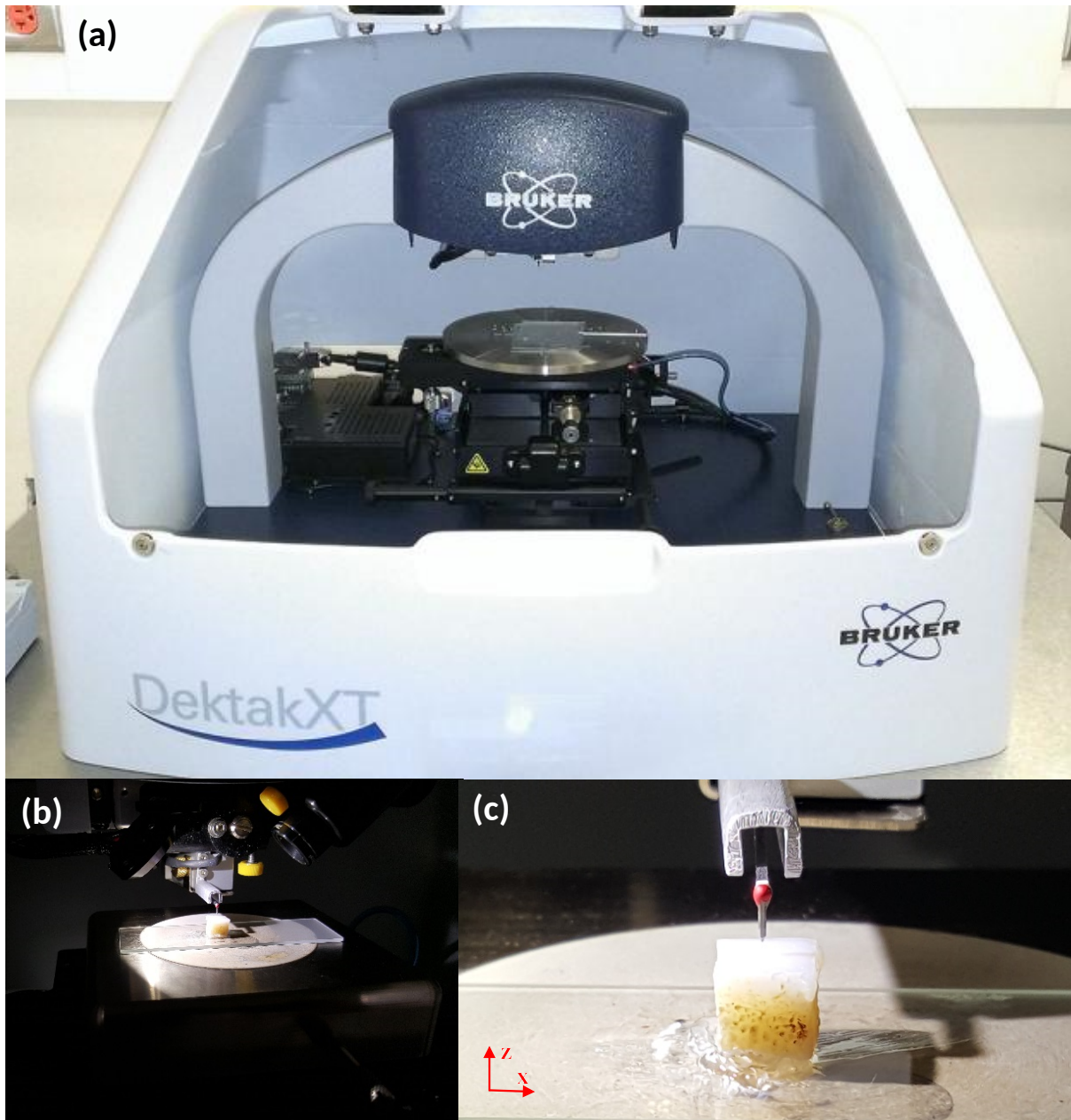
258 The cartilage surface topographies medial tibia are shown in Fig.4 and the surface
259 parameters are summarised in Table 1. Previous studies on cartilage surface
260 roughness have shown that roughness height is dependent on the size of the cartilage
261 specimen (i.e., length scale), with increasing size of a specimen, the values of R_a and
262 R_q generally increase. For small length scales which are less than 50 μm, R_q is
263 measured in hundreds of nanometres. For example, Lee et al. (2012) measured

264 human femoral heads ($40\ \mu\text{m} \times 40\ \mu\text{m}$) with different osteoarthritis stages and it is
265 showed that the values of R_q were in a range of 137 nm to 533 nm. In addition, the
266 study of Graindorge et al. (2006) on $250\ \mu\text{m} \times 250\ \mu\text{m}$ square samples harvested from
267 healthy mature bovine knee joint showed that the values of R_a and R_q were $1.06\ \mu\text{m}$
268 and $1.32\ \mu\text{m}$, respectively. Furthermore, the measurements of the cartilage surface
269 ($702\ \mu\text{m} \times 527\ \mu\text{m}$) of 6 to 8-month-old bovine knee joints by Shekhawat et al. (2009)
270 showed that the trochlea R_a was $1.15\ \mu\text{m}$ and chondyle R_a was $0.6\ \mu\text{m}$. Later on,
271 Smyth et al. (2012) measured three types of equine joints with a length scale of 5000
272 μm . It is showed that the values of R_a for midcarpal, carpometacarpal and radiocarpal
273 joints were $2.29\ \mu\text{m}$, $1.69\ \mu\text{m}$ and $1.60\ \mu\text{m}$, respectively. Therefore, by comparison,
274 the surface roughness measurements obtained in this study ($R_a = 1.97\ \mu\text{m}$, $R_q = 2.44$
275 μm for a specimen size of $1000\ \mu\text{m} \times 1000\ \mu\text{m}$) are in reasonable agreement with
276 previous measurements.

277

278

279



280

281

282

283

284

Fig.3 – Experimental equipment and samples: (a) DektakXT, Bruker Stylus profiler; (b) Glued osteochondral blocks loaded on the stylus profiler; (c) The scanning directions and close-up view of the hydrated, glued osteochondral block and the stylus tip location.

285 **2.2.2 Synthesis of cartilage surface with random roughness**

286 Although experimental measurements can provide exact surface roughness, the
287 costs, time and workloads are tremendous especially for multiple sample statistical
288 analyses. On the other hand, the characterisation of rough surfaces can also be, more
289 conveniently, synthesised by numerical methods, by which means multiple random
290 samples can be generated swiftly with desired surface parameters. In this study, a
291 numerical procedure has been utilised to synthesise rough cartilage surfaces that
292 resemble the experimental measurements in key parameters (i.e., R_q and correlation
293 length).

294 Traditionally, the surface roughness is quantified by RMS roughness height, which
295 only describes the vertical roughness (i.e., asperity heights) (Smyth et al., 2012). In
296 order to capture the whole picture of cartilage surface roughness, another parameter
297 “correlation length” is required to describe the horizontal roughness (i.e., wavelength)
298 (Bergström et al., 2007, 2008). The correlation length represents how far apart two
299 points on the surface remain correlated. The correlation length can be determined by
300 constructing the semi-variogram for the surface. The mathematical definition of semi-
301 variogram γ is given below,

$$302 \quad \gamma(\Delta x, \Delta y) = \frac{1}{2} E \left\{ \left[z(x + \Delta x, y + \Delta y) - z(x, y) \right]^2 \right\} \quad (5)$$

303 where $z(x,y)$ is the surface heights; $E\{ \}$ is the statistical expectation operator; Δx and
304 Δy are the lag distance in two orthogonal directions. Based on the definition, if the lag
305 distance is chosen to be very small, the two points are located very closely on the
306 same bump, and hence the variogram γ value computed by Eq. (5) is small, and it
307 tends to increase with the lag distance until it reaches a bend down (i.e., transition)
308 area that the dependence of variogram on lag distance becomes diminished, which

309 indicates the two points gradually lose correlation. After that the two points are no
310 longer related and the variogram exhibits a plateau called the sill. Theoretically the lag
311 distance corresponding to this bend down area can be taken as the correlation length.
312 In this study, the semi-variograms are computed by the 3D mapping software Surfer
313 (version 15, Golder Software LLC), and the semi-variogram is fitted to an exponential
314 function, so the correlation length corresponds to the distance at which the variance
315 is 63% of the sill (Barnes, 2003).

316 As observed from the experimental results, the sample surface is primarily
317 composed of “secondary undulations” and “tertiary undulations” as per the
318 classification described by Longmore and Gardner (1975). “Secondary undulations”
319 are asperities with a length scale of 200-500 μm and an average height around 10-15
320 μm , while “tertiary undulations” are the next size lower that length scale varies from 20
321 to 40 μm , and asperity heights are 0.5-2 μm . In order to better simulate the cartilage
322 surface, the information of the secondary and tertiary length scales shall be captured.
323 This is achieved by the following steps:

- 324 1) Decompose the measured surface into secondary and tertiary undulations by
325 applying Gaussian 2nd order regression filter (see Fig.4 (a)).
- 326 2) Obtain the key surface parameters (i.e., R_q and correlation length) from both
327 secondary and tertiary undulations (see Fig.4 (a)).
- 328 3) Generate two sperate random rough surfaces with the obtained key surface
329 parameters to reflect the secondary and tertiary undulations respectively by
330 using the numerical procedures given below.
- 331 4) Superpose the synthetic secondary and tertiary undulation surfaces to form a
332 completed cartilage random rough surface (see Fig.4 (b)).

333 Random rough surfaces are usually generated by the Fast Fourier Transform (FFT)
334 method combined with the power spectra density function (Wu, 2000). According to
335 Bergström et al. (2007, 2008), a three dimensional random rough surface, described
336 by $z=z(x,y)$, can be generated using two statistical distribution functions: the height
337 probability distribution function (HDF) $P(z)$ and the auto-correlation function (ACF)
338 $R_{zz}(x,y)$. The height probability distribution function characterises how far the
339 probability of the surface heights deviate from the mean value (usually taken as $z=0$).
340 The auto-correlation function describes how strongly a certain surface height is
341 correlated to another surface height separated by the 'lag distance', by defining the
342 correlated length. In short, the HDF characterises the amplitudes of the surface
343 heights, while the ACF describes the wavelengths of the peaks and valleys of the
344 rough surfaces. It is common practice to assume both HDF and ACF follow the
345 Gaussian distribution as follows,

$$346 \quad P(z) = \frac{1}{\sqrt{2\pi\sigma^2}} \exp\left(-\frac{z^2}{2\sigma^2}\right) \quad (6)$$

$$347 \quad R_{zz}(x,y) = \sigma^2 \exp\left(-\frac{x^2}{\tau_x} - \frac{y^2}{\tau_y}\right) \quad (7)$$

348 where σ is the standard deviation, which is the RMS roughness height in this study
349 (i.e., $\sigma=R_q$). τ_x and τ_y are the correlation lengths in x and y directions respectively. As
350 stated above, the correlation lengths are computed by constructing the semi-
351 variograms shown in Fig.4 (a), in which isotropic correlation lengths of 100 μ m and
352 20 μ m are obtained from the secondary and tertiary undulations respectively.

353 With HDF and ACF defined, the method given by Hu and Tonder (1992) is followed
354 to generate the random surface roughness. The procedures are briefly described
355 below.

356 On discrete mesh points of the x-y plane, a series of uncorrelated but normally
 357 distributed random surface heights $\{\eta_{x,y}\}$ ($N \times M$, in which N and M are the number of
 358 surfaces points in x and y directions respectively) are generated by Eq. (6) with a given
 359 mean value ($z = 0$) and standard deviation σ .

360 Performing the 2D FFT of $\eta_{x,y}$ yields the frequency contents (or the wavelength
 361 information) of the series $\eta_{x,y}$ denoted by $A(\omega_x, \omega_y)$.

$$362 \quad A(\omega_x, \omega_y) = \sum_{n=0}^{N-1} \sum_{m=0}^{M-1} \eta_{x,y} \cdot e^{-ik\omega_x} \cdot e^{-ik\omega_y}, \quad (\omega_x = \frac{2\pi n}{N}, \omega_y = \frac{2\pi m}{M}) \quad (8)$$

363
 364 The power spectral density function of $\eta_{x,y}$ is given by Eq. (9),

$$365 \quad S_{\eta\eta}(\omega_x, \omega_y) = |A(\omega_x, \omega_y)|^2 \quad (9)$$

366 where k and l are variable integers from 0 to $N-1$ and $M-1$ respectively.

367 Computing the 2D FFT of the ACF $R_{zz}(x,y)$ gives the power spectra density function
 368 of the rough surface heights $S_{zz}(\omega_x, \omega_y)$ in Eq. (10)

$$369 \quad S_{zz}(\omega_x, \omega_y) = \sum_{n=0}^{N-1} \sum_{m=0}^{M-1} R_{zz}(x, y) \cdot e^{-ik\omega_x} \cdot e^{-ik\omega_y} \quad (10)$$

370 The frequency contents (or the wavelength information) of the correlated rough
 371 surface $Z(\omega_x, \omega_y)$ can be obtained by computing the complex products of two series
 372 $A(\omega_x, \omega_y)$ and $H(\omega_x, \omega_y)$, where $H(\omega_x, \omega_y)$ is the transfer function of the system that is
 373 shown in Eq. (11).

$$374 \quad H(\omega_x, \omega_y) = \sqrt{\frac{S_{zz}(\omega_x, \omega_y)}{S_{\eta\eta}(\omega_x, \omega_y)}} \quad (11)$$

$$375 \quad Z(\omega_x, \omega_y) = H(\omega_x, \omega_y) \cdot A(\omega_x, \omega_y)$$

376 Finally, the correlated normally distributed rough surface heights can be computed
 377 by an inverse fast fourier transform (IFFT) of $Z(\omega_x, \omega_y)$.

377
$$z(x, y) = \frac{1}{NM} \sum_{n=0}^{N-1} \sum_{m=0}^{M-1} Z(\omega_x, \omega_y) \cdot e^{ik\omega_x} \cdot e^{ik\omega_y} \quad (12)$$

378 The algorithm has been implemented in MATLAB (R2017b, The MathWorks, Inc.).
 379 10 samples were generated for cartilage on medial tibia. The comparison of surface
 380 parameters is summarised in Table 1. Additionally, the synthetic rough surfaces with
 381 the closest R_q values out of the 10 samples to the corresponding experimental
 382 measurements is plotted in Fig.4 (b).

383 Generally, the key parameters of the synthesised surfaces match well with the
 384 experimental measurements, especially for the averaged roughness R_a and RMS
 385 roughness R_q values. The maximum differences are less than 1%. It should be noted
 386 that the mathematical algorithm is a pseudo-random process and hence the synthetic
 387 rough surfaces exhibit more evenly distributed values for surface peaks and valleys
 388 than the measured samples. Therefore, there are small discrepancies for the
 389 comparison of the maximum peak height R_p and maximum valley depth R_v . This is
 390 believed to be caused by the sample sizes. With larger sample sizes, the key
 391 parameters can be captured more accurately. However, 10 samples are considered
 392 sufficient in this study to satisfy statistical requirements based on the standard
 393 deviation convergence tests for viscosity and permeability in Section 3.2.

394 **Table 1 – Surface roughness parameter comparisons between experiment and**
 395 **synthetisation**

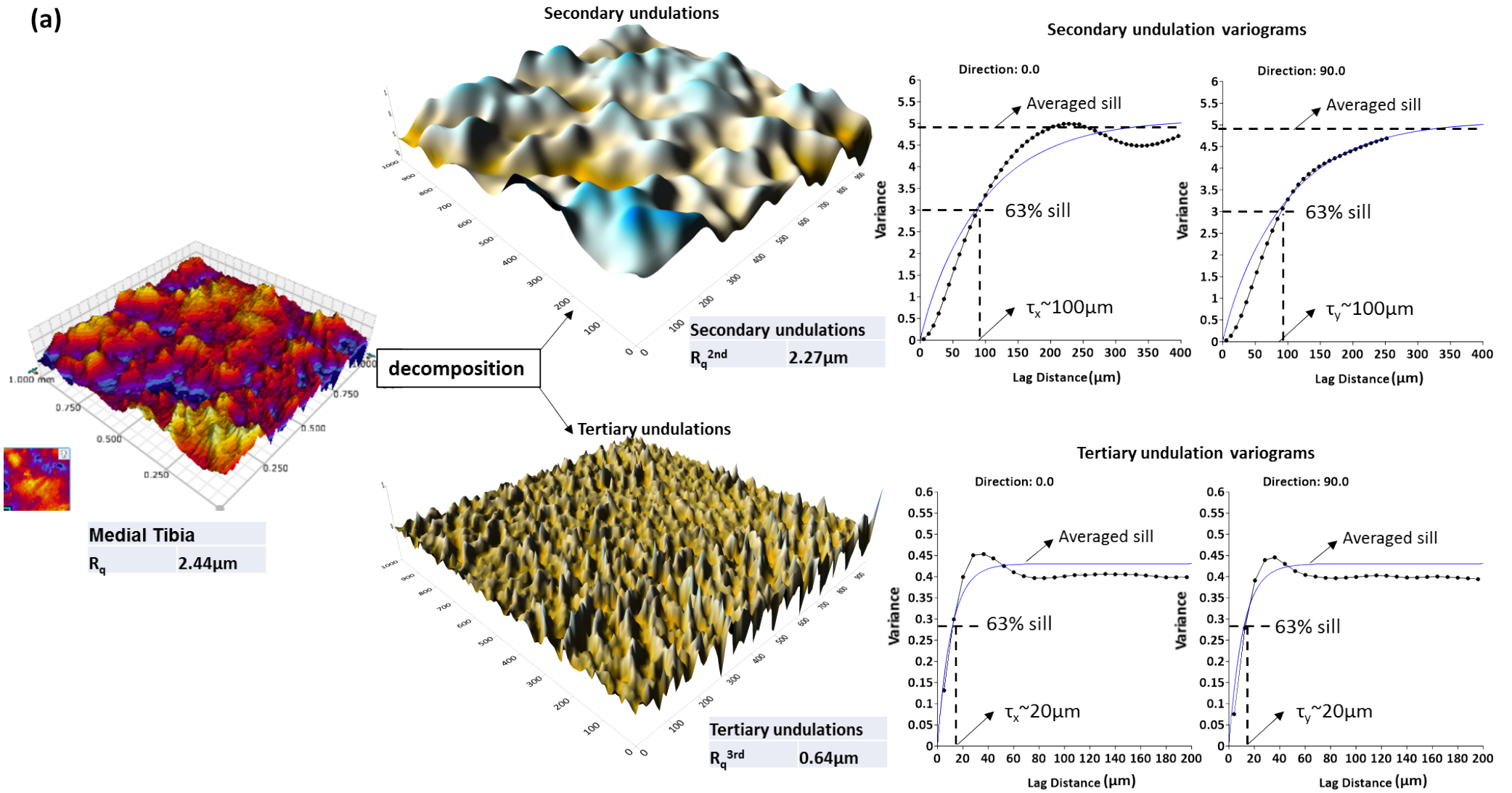
Surface parameter	Medial Tibia	
	Experiment	Synthetisation*
R_a (μm)	1.97	1.94 (0.069)
R_q (μm)	2.44	2.42 (0.074)
R_p (μm)	8.83	7.66 (0.313)
R_v (μm)	-13.92	-7.29 (0.756)
R_t (μm)	22.75	14.95 (0.723)

*values outside the brackets are means, inside the brackets are standard derivations ($n = 10$).

396

397

(a)

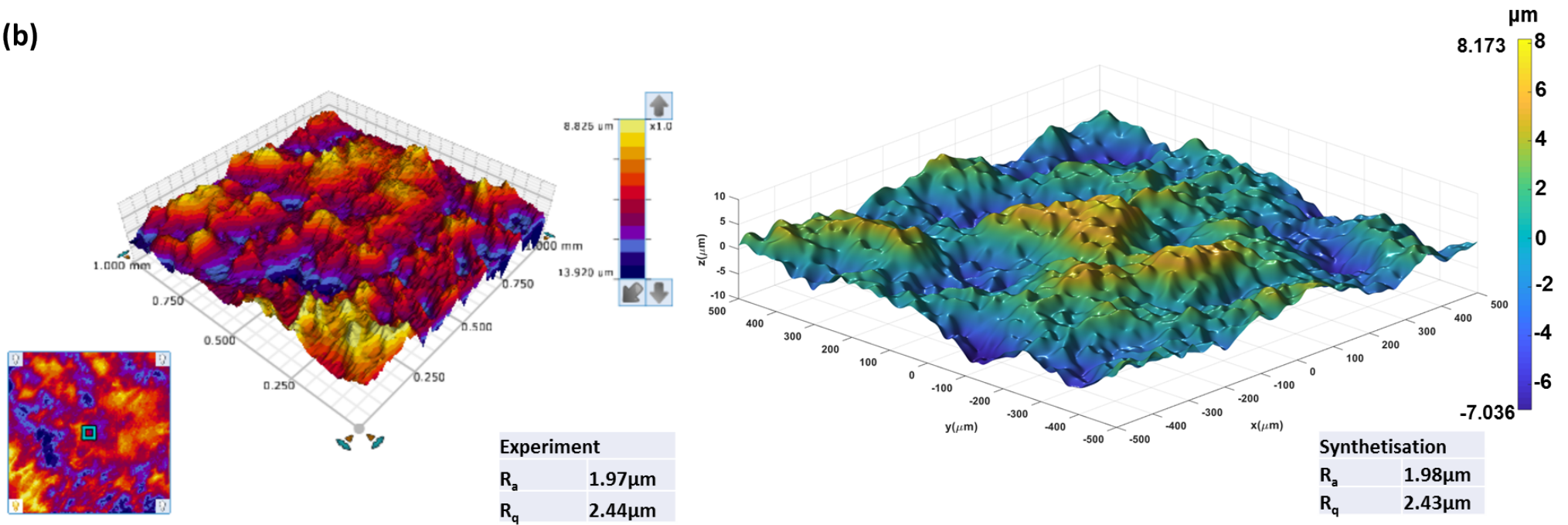


398

399

400

(b)



401

402

403

404

Fig.4 – Synthesise cartilage rough surfaces based on experimental measurements: (a) Decomposed secondary & tertiary undulations and variograms in two orthogonal directions; (b) Cartilage topography and synthesised random rough surface.

405 **2.3 Numerical analysis of contact gap flow**

406 **2.3.1 Model description**

407 The simulations of fluid flow within the gap between rough opposing surfaces were
408 performed in COMSOL Multiphysics (version 5.3, COMSOL, Inc.). A typical micro-
409 scale REV is shown in Fig.5 (a). The random rough surfaces (lower wall) generated
410 above were imported to COMSOL.

411 The upstream and downstream walls (highlighted in blue) in the x direction were
412 defined as inlet and outlet boundaries, respectively. The two lateral walls (highlighted
413 in yellow) in the y direction were symmetrical boundaries parallel to the flow to form a
414 continue pore space. The lower surface representing the cartilage roughness in z
415 direction was assigned no-slip boundary. In addition, the upper wall in z direction was
416 defined as symmetry boundary to simulate two symmetrical cartilage contact. Fluid-
417 structure interactions between the gap flow and the asperities were not considered, as
418 it is probably a minor effect and not the primary focus of this study.

419 However, the analyses did consider the consolidation of the asperities in the pore
420 spaces. Consolidation of the asperities alters the size and shape of the gap. Since the
421 Poisson's ratio of the cartilage extracellular matrix often approaches zero (Mow et al.,
422 1993), especially in deformation rate regimes in which the interstitial fluid within the
423 asperity has time to leave the tissue (there is fast consolidation as a result of the short
424 asperity drainage path length)). It is convenient to approximate the gap closure
425 geometry by just lowering down the contact plane to intersect with the asperities at
426 varies heights (i.e., at 8, 6, 4, 2 and 0.5 μm for a single cartilage, which corresponds
427 to the total gap heights of 16, 12, 8, 4 and 1 μm respectively for the contact of two
428 cartilages with the same topography). The cartilage surface roughness at varies
429 heights and degrees of contact are shown in Fig.5 (c). Separate models were created

430 for each gap height, and for each gap model, various inlet pressures, ranging from
431 100 to 10000 Pa, together with the outlet pressure set at zero Pascal were applied.

432 Laminar, incompressible and isothermal flow was assumed in the gap for the micro-
433 scale REV models. Stationary Navier-Stokes equations were solved by the
434 generalised minimal residual method (GMERS) for each gap model at each inlet
435 pressure.

436 **2.3.2 Viscosity of synovial fluid**

437 Synovial fluid is a semidilute hyaluronate (HA) and protein solution with a density
438 of 1225 kg/m^3 , the viscosity of which exhibits non-Newtonian shear rate dependent
439 characteristics. The viscosity of synovial fluid will affect the flow velocity in the gap.
440 The rheology of synovial fluid has been studied extensively (Fam et al., 2007). The
441 experimental results by Schurz and Ribitsch (1987) showed the zero-shear rate
442 viscosity (μ_0) ranges for healthy synovial fluid were 1-40 Pa·s. After a Newtonian
443 plateau at shear rate around $0.05\text{-}0.1 \text{ s}^{-1}$, synovial fluid exhibited shear thinning
444 behaviour up to shear rate of 1000 s^{-1} where the reported experimental data
445 terminated, at which the corresponding viscosity for healthy synovial fluid is 0.009
446 Pa·s.

447 The generalised Newtonian constitutive equations have been used to capture
448 the non-Newtonian behaviour of synovial fluid. The curve-fitting power law equation
449 reported by Lai et al. (1978) indicated that a normal synovial fluid would reach the
450 infinite shear viscosity (μ_∞) around $0.007\text{-}0.01 \text{ Pa}\cdot\text{s}$ for high shear rates more than
451 1000 s^{-1} .

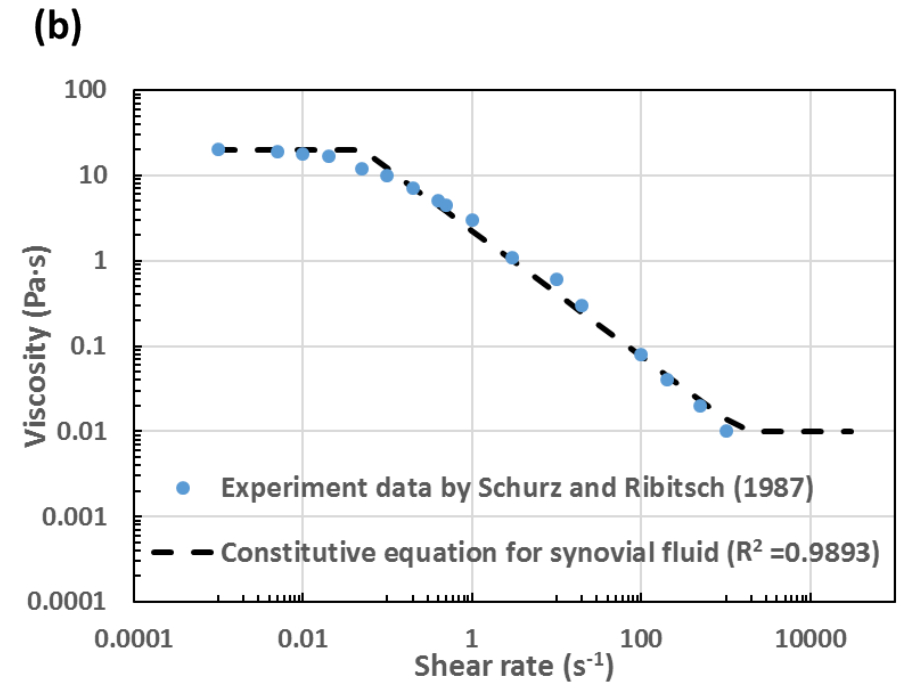
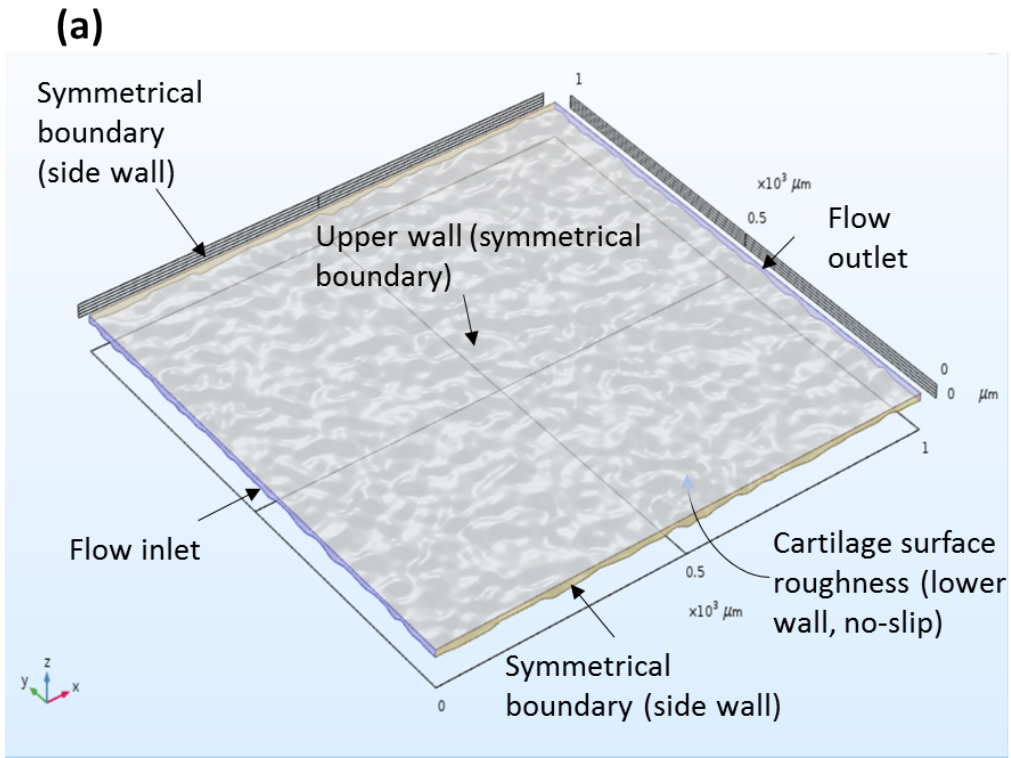
452 The present study combined the findings of these two studies (Schurz and
453 Ribitsch, 1987; Lai et al., 1978) and utilised a tri-linear model to approximate the

454 experimental data of the healthy synovial fluid by Schurz and Ribitsch (1987), in
 455 which the shear thinning was approximated by a power law equation between the
 456 two Newtonian plateaus of zero-shear viscosity $\mu_0 = 20.3 \text{ Pa}\cdot\text{s}$ and infinite-shear
 457 viscosity $\mu_\infty = 0.01 \text{ Pa}\cdot\text{s}$ as per Lai et al. (1978). The equation is present below and
 458 plotted in Fig.5 (b) for comparison.

$$459 \quad \mu(\text{Pa}\cdot\text{s}) = \begin{cases} 20.3 & , \quad (\dot{\gamma} \leq 0.05\text{s}^{-1}) \\ m\dot{\gamma}^{n-1} (m = 2.237, n = 0.263) & , \quad (0.05\text{s}^{-1} \leq \dot{\gamma} \leq 1000\text{s}^{-1}) \\ 0.01 & , \quad (\dot{\gamma} \geq 1000\text{s}^{-1}) \end{cases} \quad (13)$$

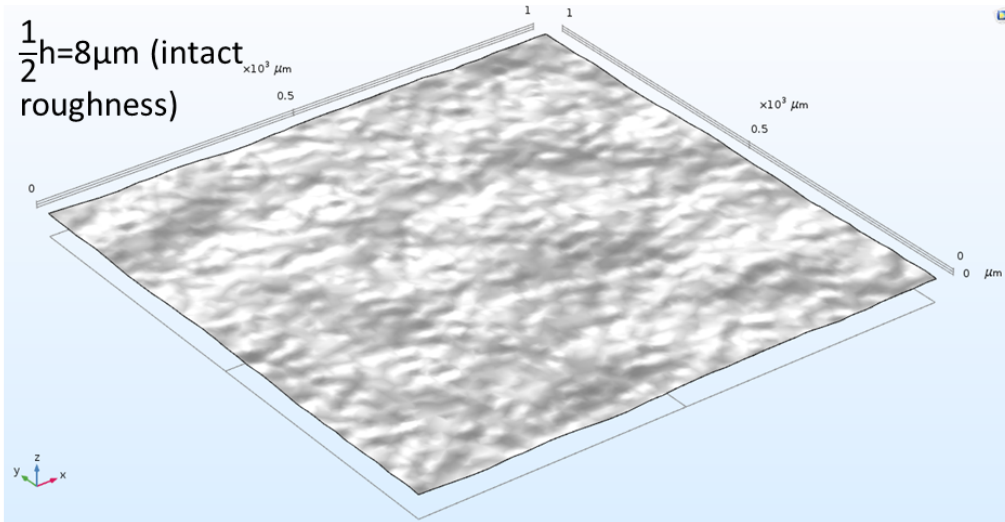
460 It should be noted that the experimental data measured by viscometers is usually
 461 from steady state oscillating flow, as the synovial fluid samples are usually pre-
 462 sheared for a few minutes before testing. The oscillating shear test is not exactly
 463 the same as the conditions in a joint, but it is probably the closest representation
 464 for a cyclically loaded joint.

465

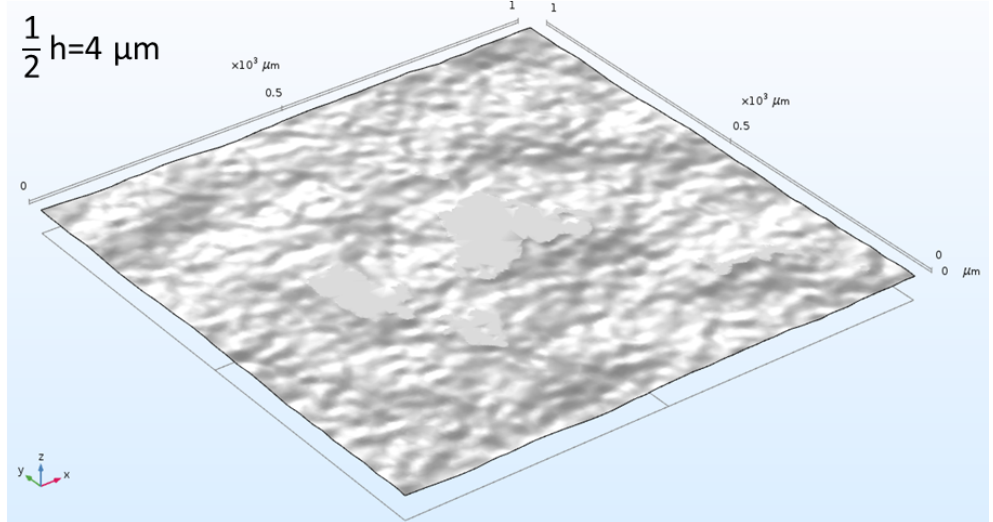


(c)

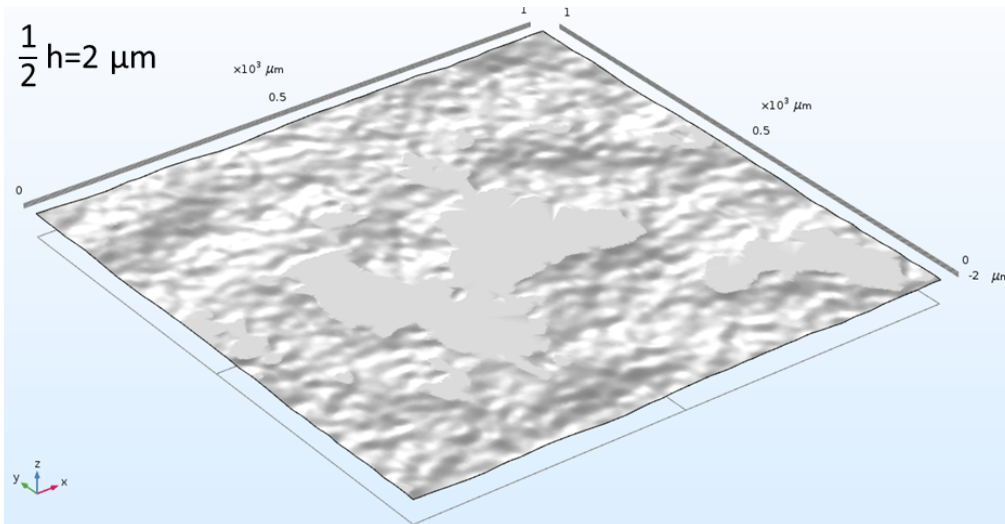
$\frac{1}{2}h=8\mu\text{m}$ (intact roughness)



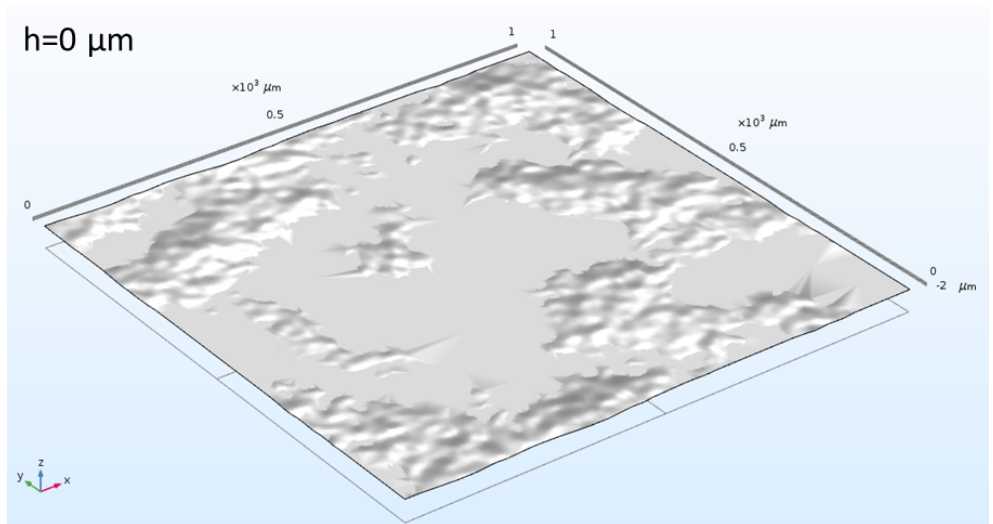
$\frac{1}{2}h=4\mu\text{m}$



$\frac{1}{2}h=2\mu\text{m}$



$h=0\mu\text{m}$



467

468

469

Fig.5 – Numerical analyses setup: (a) A typical micro-scale REV model for CFD analyses; (b) Comparison of synovial fluid constitutive equation with experimental data; (c) Shapes of the cartilage surface roughness at different gap heights.

470 **3 RESULTS AND DISCUSSION**

471 **3.1 Initial tests**

472 Initial testing was performed for the purposes of result comparison and model
473 verification against the previous findings.

474 The initial analysis inputs were set as close as possible to mimic Wu and Ferguson
475 (2017) simulations, i.e., fluid domain was set as $80\ \mu\text{m} \times 80\ \mu\text{m}$, RMS roughness R_q
476 = $0.5\ \mu\text{m}$, inlet pressure was 400 Pa, outlet pressure was 0 Pa and fluid viscosity was
477 $1\ \text{Pa}\cdot\text{s}$. However, the wavelength information was not provided, to this end, three
478 surfaces with different correlation lengths (i.e., $\tau = 2, 4$ and $6\ \mu\text{m}$) were generated
479 for comparison.

480 The volumetric averaged velocities were output at various gap heights. The gap
481 permeability K_r was calculated using Eq. (4) and results are plotted in Fig.6 for
482 comparison. As viscosity is constant, K_r is only related to the intrinsic permeability κ
483 which is a function of pore size (i.e., gap height h). It is shown that generally the results
484 of initial tests match closely with Wu and Ferguson (2017) both in trend and absolute
485 value. Through the calibration process, it is shown that the results of $\tau = 6\ \mu\text{m}$ match
486 the most closely to the results of Wu and Ferguson (2017) (less than 4% difference).

487 Another noticeable trend is that surfaces with smaller correlation lengths tend to
488 have better fluid retention capability. This is because under the same REV size and
489 R_q , smaller correlation lengths generate more undulations that enlengthens the
490 drainage path. The results underline the importance of considering the two correlation
491 lengths in the model.

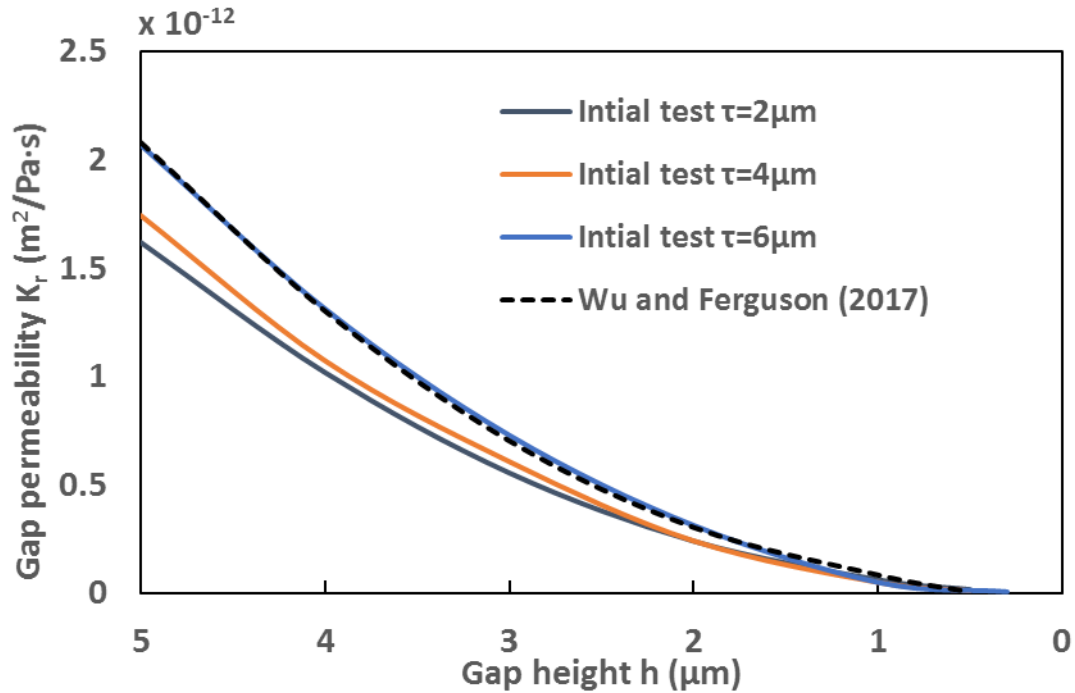


Fig.6 – Model verification against Wu and Ferguson (2017).

492
493
494

3.2 Fluid viscosity

496 As stated previously, viscosity is a function shear rate and so will depend on
497 both the gap height and the fluid velocity. Since the fluid velocity is driven by the
498 fluid pressure gradient $\Delta p/\Delta r$, viscosity is also dependent on the fluid pressure
499 gradient, such that it can be expressed as $\mu = \mu(h, \Delta p/\Delta r)$. The apparent viscosity
500 as a function of the pressure gradient and gap height is shown in Fig.7 in log-log
501 scale, in which the dashlines are extrapolations to the infinite-shear viscosity $\mu_\infty =$
502 0.01 Pa·s. The viscosity charts are plotted by the mean values of the 10 surface
503 samples generated previously, and the error bars are the standard deviations.
504 Incremental convergence tests for the standard deviations were performed for the
505 most divergent case ($h = 1 \mu\text{m}$) at all pressure gradients, and the results show that
506 the standard deviations at all pressure gradients decrease with increasing surface
507 sample size and gradually become constant. When the sample sizes are increased

508 to 10, the differences of the standard deviation of the viscosity at all pressure
509 gradients compared to 9 samples are reduced to 5%. Therefore, in this study 10
510 samples are sufficient to satisfy statistical requirements.

511 As shown, for a fixed pressure gradient, the fluid viscosity increases as the gap
512 narrows. For example, under the same pressure gradient of 10^7 Pa/m, viscosities
513 for the gap height of 16 and 12 μm have already reached the infinite-shear viscosity
514 $\mu_\infty = 0.01$ Pa·s, while the viscosity for $h = 4$ μm is 100 times higher (i.e., 1 Pa·s).
515 Furthermore, the viscosity decreases with increasing fluid pressure gradient (or
516 fluid velocity). For example, by increasing the inlet pressure by 1000 times from the
517 shear thinning threshold, the viscosities of gap heights of 4 μm would reduce from
518 the maximum μ_0 to the minimum μ_∞ . The results demonstrate that the effect of a
519 shear rate dependent viscosity potentially plays a significant role in fluid flow
520 through the gap and so is joint lubrication.

521 Using a constant viscosity of 1 Pa·s or 0.6 Pa·s may reflect the general fluid
522 behaviour in the gap, but it fails to capture the synovial fluid behaviour during the
523 joint contact as a process. For a single load event, such as standing up, after a
524 quick squeeze-film stage, the rough surfaces of the upper and lower cartilages will
525 come into contact. When the contact initiates, the total applied load σ_t (i.e., body
526 weight) is initially resisted by the fluid pressure p in the gap only. In this instance, the
527 initial viscosity of synovial fluid is expected to be high, as it takes some time for the
528 long molecules in the fluid to re-orientate. Once the relaxation time passes, the
529 synovial fluid begins to thin and eventually reaches a steady state similar to the
530 viscometer experiments. Now in an early contact stage, the majority of the load is
531 taken up by the fluid and hence the fluid pressure gradient is high, the viscosity of
532 the fluid is low and may be close to the infinite shear viscosity. As a result, the fluid

533 exits the gap quickly while it closes. With the closure of the gap, the surface asperities
534 start to consolidate and the contact stress σ_c will rise and take up the total applied load
535 as per Eq. (14),

$$536 \quad \sigma_t = \sigma_c + p \quad (14)$$

537 As the asperity consolidation continues, both the gap height and the fluid pressure
538 gradient will reduce, the viscosity of the remaining synovial fluid will increase as per
539 Fig.7. Therefore, the fluid flow process in temporal cartilage contact is complex, and
540 this complexity cannot be accurately captured by using a constant viscosity value.

541 **3.3 Gap permeability**

542 The gap permeability K_r was computed by Eq. (4) and plotted in Fig.8 using a log-
543 log scale. The similar convergence study using $h = 1 \mu\text{m}$ case as example was carried
544 out to determine the sample size required to estimate the K_r . The results also show
545 that 10 samples of rough random surfaces are sufficient to satisfy statistical
546 requirements (less than 5% change in standard deviation).

547 K_r is also a function of gap height and fluid pressure gradient because $K_r =$
548 $\kappa(h)/\mu(h, \Delta p/\Delta r)$. As expected, gap permeability reduces with gap closure due to
549 the reduction in pore space. It is also apparent that gap permeability is very sensitive
550 to the fluid pressure gradient, e.g. at gap height of $8 \mu\text{m}$, the 10 times decrease in
551 pressure gradient (from 10^7 to 10^6 Pa/m) could lead to a 600 fold decrease in gap
552 permeability.

553 The gap fluid flow velocity can be found by multiplying the pressure gradient in
554 X-axis to the corresponding gap permeability values in Y-axis (as per Eq. (1)).
555 Moghadam et al. (2014) developed a numerical model to compute the synovial fluid
556 flow between two cartilage surfaces under sinusoidal deformation (at 15 Hz and

557 15% strain amplitude). In their study the viscosity was kept constant at 0.6 Pa·s.
558 They predicted that the maximum flow velocity between two contacting cartilages
559 was around 120-180 $\mu\text{m/s}$. To compare results using Fig.7 and Fig.8, if we assume
560 that the 15% cartilage strain in their study corresponds approximately to 15%
561 roughness strain in the present study (i.e., $h = 14 \mu\text{m}$, take an interpolation between
562 $h = 16$ and $12 \mu\text{m}$ curves). The reading of pressure gradient corresponding to 0.6
563 Pa·s from Fig.7 (i.e., around $1.2 \times 10^6 \text{ Pa/m}$), multiplied by the corresponding gap
564 permeability from Fig.8 (i.e., around $1.7 \times 10^{-11} \text{ m}^2/\text{Pa}\cdot\text{s}$), yields a gap flow velocity
565 around 200 $\mu\text{m/s}$, which matches reasonably with Moghadam et al. (2014). In
566 addition, another study by Chen et al. (2011) determined the interfacial flow velocity
567 ranged from 26 to 65 $\mu\text{m/s}$, it should be noted that the flow velocity in Chen's study
568 was obtained from the upmost layer of a tissue engineered cartilage hydrogel that
569 formed on top of the cartilage surface, in which the presence of molecules in the
570 gel and the concentration of synovial fluid are expected to provide additional
571 resistance to the flow. However, this study mainly focuses on the fluid flow from
572 mechanical perspective and hence our prediction tends to be 3 to 7 times greater.

573 Another observation from Fig.8 is that the error bars (mean + standard derivation)
574 become more and more divergent with gap closure. When contact initiates, K_r values
575 are relatively convergent regardless of different sample topographies, which indicates
576 at this stage K_r is insensitivity to the variation of cartilage surface topography. This is
577 because the formation of the roughness is assumed to follow the Gaussian distribution
578 that the majority (around 68%) of the asperity heights would distribute in an interval of
579 one standard deviation from the mean (around $h = 5 \mu\text{m}$). While in the early contact
580 stage (i.e., $h = 16$ to $12 \mu\text{m}$) only a few highest asperities are connected and so a
581 relatively generous gap still exists between the highest asperities and the majority of

582 surface roughness, from which most of fluid can more easily escape. With the contact
583 continues, K_r values become more and more sensitive to the surface topography,
584 because the flow heterogeneity become increasingly significant due to gap closure,
585 especially when the positive roughness peaks are almost flattened (i.e., $h = 4$ and 1
586 μm), and fluid flow is forced to take the increasingly tortuous paths in the remaining
587 connected negative roughness pore spaces. Therefore, the cartilage surface
588 topography has increasing influences on the gap permeability when the contact gap
589 closes.

590 Fig.8 also provides an index to evaluate the gap permeability. The maximum K_r
591 are capped by the corresponding values when the viscosity of each gap height
592 reaches the infinite-shear viscosity limit of $0.01 \text{ Pa}\cdot\text{s}$, as the fluid viscosity is no
593 longer dependent on the pressure gradient. To the knowledge of the authors,
594 currently there is no effective experimental method to measure the gap permeability
595 either *in vivo* or *in vitro*. However, the pressure gradient and gap height can be
596 quantified with advanced equipment. The cartilage contact pressure contours have
597 been mapped by some researchers with modified endoprosthesis integrated with
598 transducers (Rushfeldt et al., 1981), Tekscan knee sensor (Marzo and Gurske-
599 DePerio, 2009) and most recently with 3D laser scanning (De Santis et al., 2018).
600 As 95% of the contact loadings is assumed supported by the interstitial fluid, due
601 to fluid pressure continuity, it is reasonable to assume 95% of cartilage contact
602 pressure is supported by the gap fluid pressure (Wu and Ferguson, 2017). On the
603 other hand, the measurement of gap thickness for stainless steel on glass in calf serum
604 was also made possible with a commercial optical interferometric tribometer (Myant
605 and Cann, 2013). Therefore, with experimental devices existing for in principle

606 measurement of quantified fluid pressure gradient and gap thickness, gap permeability
607 may be evaluated indirectly in the future using Fig.8.

608 Several recent studies have investigated the formulations of cartilage contact during
609 mixed mode lubrication. For example, Sokoloff (2012) modelled the fluid flow in the
610 contact gap by Darcy's law, and hence the gap permeability is required as a key input
611 parameter. Thus, the current study could lead to a more realistic gap permeability
612 estimation. In addition, the formulations of cartilage mixed mode contact are complex
613 because a more complete model should consider the asperity contact and fluid
614 exchange between interstitial fluid in cartilage tissue driven by the pressure difference
615 between the gap and cartilage asperity tissue, rather than assumed equilibrium
616 conditions. A more realistic model would also consider the fluid connection to the
617 underlying cartilage tissue. We plan to extend the gap model to include the underlying
618 cartilage tissue in a future study. This study numerically predicts the gap permeability
619 against a range of gap sizes and fluid pressure gradients in the gap. The outcomes of
620 this study could potentially contribute to the development of more realistic models in
621 the future. A future study will connect this gap with a cartilage bulk deformation model,
622 which should result in a model that is closer to "real world behaviour" occurring in
623 synovial joints.

624 In summary, this study adopts a displacement-based approach to simulate synovial
625 fluid flow in the contact gap during the gap closure. The purpose of this study is mainly
626 to investigate the non-Newtonian fluid behaviour in the contact gap between two
627 cartilages, under different fluid pressure gradients (representing the fluid pressure in
628 the gap resulting from different load conditions and stages) and gap sizes (i.e., asperity
629 level deformation). The results suggest that the contact gap flow is governed by a
630 combined effect of surface roughness, synovial fluid properties and fluid pressure

631 gradient. The presence of roughness in the gap not only changes the intrinsic
632 permeability (i.e., the pore spaces in the gap) as per Wu and Ferguson (2017), in a
633 more realistic physiological condition (i.e., non-Newtonian behaviour of synovial fluid),
634 under the change of fluid pressure in the contact gap, cartilage surface roughness
635 could also increase fluid local shearing which can alter the viscosity of synovial fluid,
636 and thereby influence the gap permeability.

637 **3.4 Discussion on joint lubrication**

638 The permeability values of cartilage and the gap can shed some light on the
639 plausibility of joint lubrication theories in the mixed mode regime. The bulk permeability
640 of cartilage, dependent on the concentration of aggrecan, is normally in the range of
641 10^{-15} - 10^{-16} m²/Pa·s (Miramini et al., 2017). The permeability at the top surface as a
642 collagen dominant area would be expected to be less than the average
643 permeability, but the increasing actual concentration of aggrecan in a cartilage
644 consolidation process will also reduce the initial cartilage permeability. With this
645 understanding, it is reasonable to take 10^{-15} m²/Pa·s as a reference for comparison.

646 The results in Fig.8 show that when the gap height reduces to less than 1 μm
647 and fluid pressure gradient reduces below 5×10^5 Pa/m, the gap permeability would
648 drop to the order of 10^{-15} m²/Pa·s. Therefore, we may tentatively define the following
649 lubrication regimes: (1) from the initial contact to the positive roughness (peaks)
650 being completely flattened (i.e., $h = 0$) as the mixed mode lubrication regime; (2)
651 $h=0$ to be the onset of boundary only lubrication regime (end of the mixed mode);
652 (3) in the mixed mode regime, when gap permeability reduces to the order of 10^{-15}
653 m²/Pa·s, that is the same as cartilage tissue, weeping lubrication probably shifts to
654 boosted lubrication, then a more clear picture of the lubrication process during
655 contact begins to emerge. Weeping is likely to be the primary lubrication

656 mechanism in mixed mode, as for most of the gap closure the gap permeability is
657 much greater than that of the underlying cartilage. This will cause the gap fluid to
658 exit laterally into the capsule. With contact area increasing, connected porosity
659 decreases to such an extent that boosted lubrication is likely to become dominant
660 over weeping lubrication at some point, probably around the point when
661 permeability of the gap is approximately equal to the cartilage tissue (e.g. when h
662 = 1 μm and pressure gradient reduces to less than 5×10^5 Pa/m in this study). The
663 boosted lubrication tends to dominate at the end of mixed mode regime, and it
664 leaves a layer of concentrated protein gel as boundary lubricant that aids boundary
665 lubrication. Therefore, this boosted lubrication regime extends the duration of the
666 mixed mode lubrication regime, further delaying the onset of the boundary (only)
667 lubrication regime. At this turning point when permeability of the gap is equal to the
668 cartilage tissue (i.e., $h = 1 \mu\text{m}$ and pressure gradient reduces to less than 5×10^5
669 Pa/m in this study), it can be defined that the gap is functionally closed.

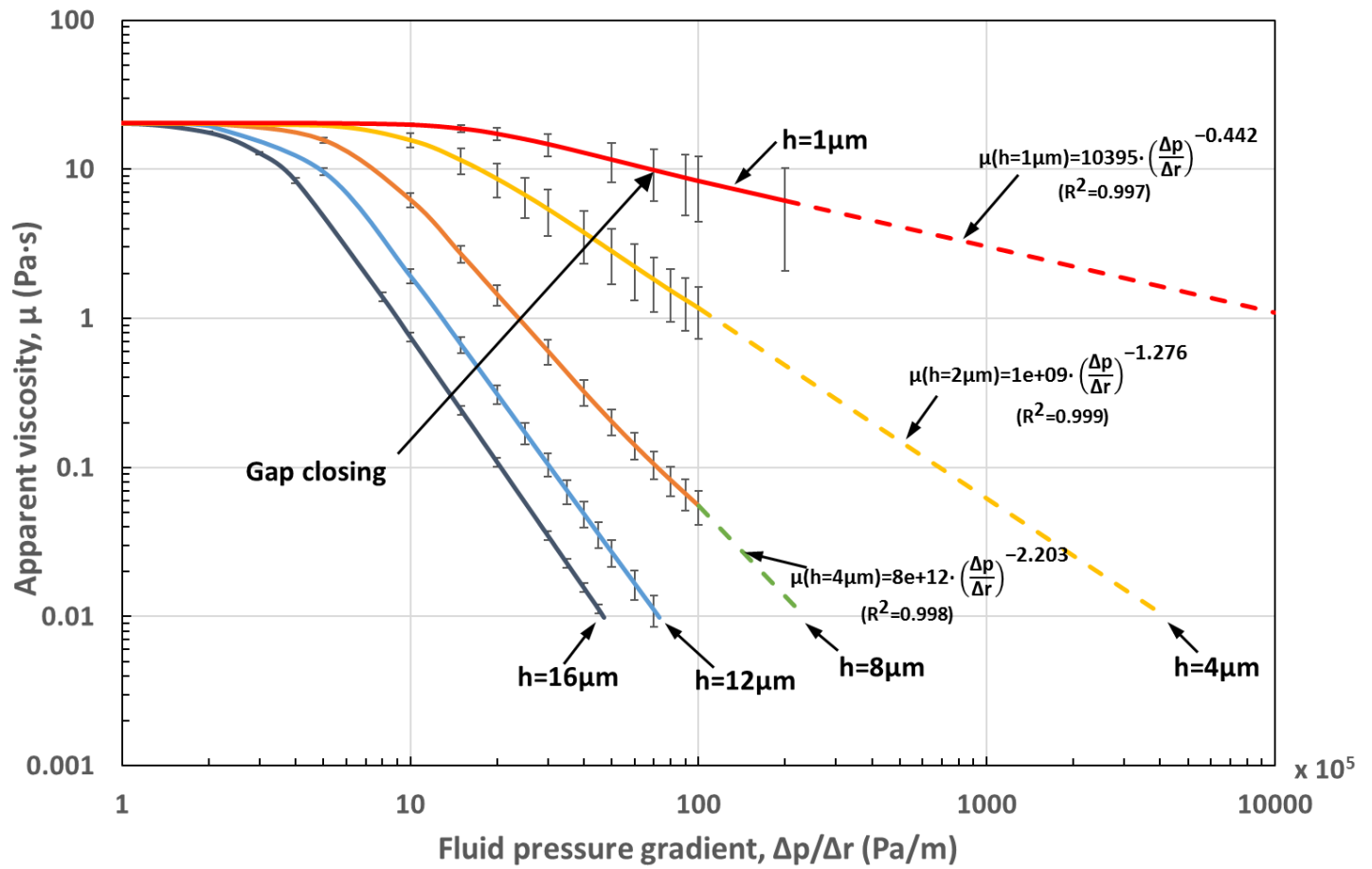
670 In addition, as shown in Fig.5 (b), when the gap height reduces to zero, the fluid
671 trapped in the valleys of the roughness become isolated, disconnected pools with an
672 average volume of 950940 μm^3 (out of the 10 samples), which is around 13% of the
673 volume for the initial gap at first contact. This means that around about 13% of the
674 total fluid in the gap might experience ultrafiltration (boosted lubrication), while
675 around 87% of the fluid in the gap would be extruded along the gap to the capsule
676 (weeping lubrication).

677 It should be mentioned that the proposed definition above on gap functional closure
678 is a local criterion. The uneven distribution of interstitial fluid could generate non-
679 uniform cartilage deformation and different gap sizes in different locations, which
680 implies that the fluid exchange (weeping and boosted) in the gap is spatially and locally

681 variable. In other words, it is possible for different parts of the gap to be in different
682 lubrication modes. Limitations of this study should be emphasised. Additional to
683 relative permeability, relative path length may also influence the fluid flow from the
684 global perspective. However, the global effect of the relative path length during joint
685 contact cannot be captured in this study because the current gap model is only suitable
686 for investigating the micro-level gap flow. To consider the path length and fully unlock
687 the mystery of fluid flow between cartilage and contact gap, a global and integrated
688 cartilage contact model involving fluid flow in the contact gap, asperity level
689 deformation and cartilage tissue biphasic behaviour needs to be developed. This study
690 represents the first step towards the formulation of a comprehensive cartilage contact
691 model, and clearly further investigations are required.

692 In addition (and similar to the study of Wu and Ferguson (2017)), this study neglects
693 the bulk deformation of cartilage tissue as a first estimate of the contact gap behaviour.
694 However, role of the bulk deformation of cartilage tissue is clearly required to form an
695 integrated cartilage contact model. When under compression, the cartilage tissue will
696 deform globally, contact drainage paths may lengthen and cartilage may consolidate
697 non-uniformly. For example, in gap sizes could be different between the cartilage
698 perimeter edges where interstitial fluid can more easily exudate compared to the
699 "central area" of the cartilage where the drain paths are longer. In other words, the
700 geometry of the contact gap and the geometry of the cartilage tissue continuously
701 change, and this is not reflected in the current model. Some of these issues can be
702 addressed in future modelling studies, but further experimental work is also
703 required. For example, there is currently no experimental confirmation of how
704 surface asperities deform under load. With the aids of surface profilometer, a future

705 study may be able to establish a relationship between asperity level deformation
 706 and the cartilage bulk deformation.



707
 708 Fig.7 – Apparent viscosity at various gap heights and fluid pressure gradients

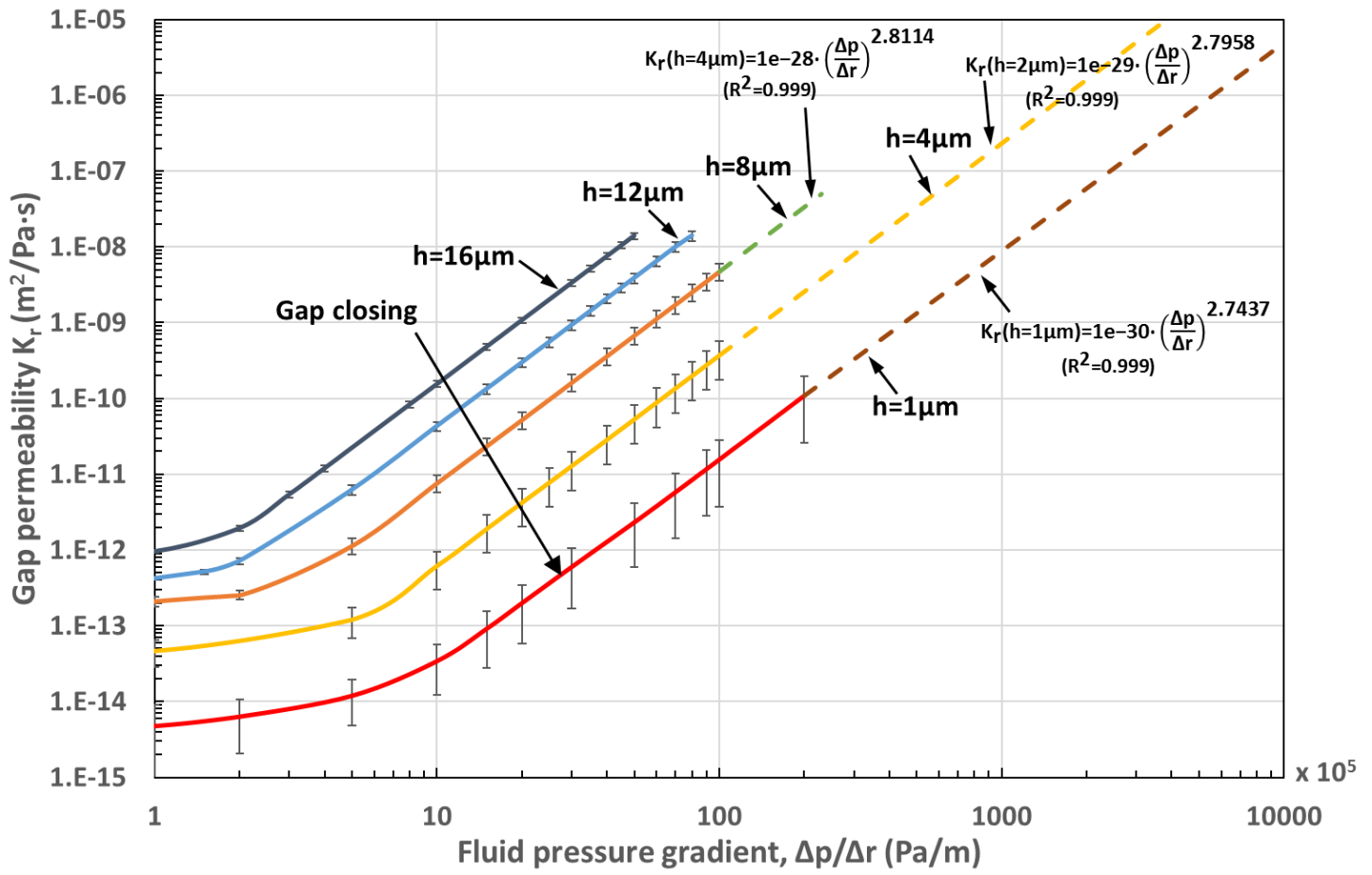


Fig.8 – Gap permeability at various gap heights and fluid pressure gradients

709
710
711
712
713
714
715
716
717
718
719
720
721
722
723

724 4 CONCLUSIONS

725 This study investigates the synovial fluid flow behaviour (i.e. permeability) in various
726 sizes of cartilage contact gap by developing CFD models and synthesising cartilage
727 surface with random roughness based on experimental measurements. The CFD
728 model is validated against the study of Wu and Ferguson (2017) and the flow
729 velocity results are consistent with other research findings (Moghadam et al.,
730 2014). The findings are summarised as follows:

- 731 • The experimental measurements of bovine media tibia cartilage and surface
732 analysis results show that the averaged roughness R_a is 1.97 μm and RMS
733 roughness R_q is 2.44 μm . The correlation lengths of the secondary and tertiary
734 undulations are round 100 μm and 20 μm , respectively.
- 735 • The gap permeability decreases as gap is closing. For example, at pressure
736 gradient of 10^6Pa/m , the decrease of gap height from 4 μm to 1 μm could result
737 in 20 fold decrease in permeability. In addition, it shows that the gap
738 permeability is very sensitive to the fluid pressure gradient, e.g. at gap height
739 of 8 μm , the 10 fold decrease in pressure gradient (from 10^7 to 10^6 Pa/m) could
740 lead to 600 fold decrease in gap permeability. The gap permeability charts
741 developed in this study can be used to estimate the gap permeability under
742 different gap heights and fluid pressure gradients.
- 743 • As the cartilage contact gap closes, the permeability of the contact gap
744 gradually approaches that of the cartilage tissue. At some point, e.g., gap
745 height is around 1 μm and fluid pressure gradient is below 5×10^5 Pa/m, the
746 contact gap may be defined as being “functional closed”, as the gap
747 permeability becomes approximately equal to the permeability of the

748 cartilage tissue. This suggests that weeping lubrication is the primary mode
749 when gap height and fluid pressure when the contact gap is functionally
750 open, and boosted lubrication becomes significant when the contact gap is
751 functionally closed.

752

753 **Acknowledgements**

754 The authors acknowledge the funding support from The Australian Research
755 Council (DP180100915) and The University of Melbourne.

757 **REFERENCES**

- 758 Ateshian, G.A., 2009. The role of interstitial fluid pressurization in articular cartilage lubrication.
759 J Biomech 42, 1163-1176.
- 760 Barnes, R., 2003. Variogram tutorial. Golden Software.
- 761 Bear, J., 1988. Dynamics of fluid in porous media. Dover Publication, New York.
- 762 Bergstrom, D., Powell, J., Kaplan, A.F.H., 2007. A ray-tracing analysis of the absorption of
763 light by smooth and rough metal surfaces. J. Appl. Phys. 101, 113504.
764 <https://doi.org/10.1063/1.2738417>.
- 765 Bergstrom, D., Powell, J., Kaplan, A.F.H., 2008. The absorption of light by rough metal
766 surfaces - A three-dimensional ray-tracing analysis. J. Appl. Phys. 103, 103515.
767 <https://doi.org/10.1063/1.2930808>.
- 768 Bhuanantanondh, P., 2009. Rheology of synovial fluid with and without viscosupplements in
769 patients with osteoarthritis: A pilot study. Mater Degree Thesis. The University of British
770 Columbia.
- 771 Bujurke, N.M., Kudenatti, R.B., 2006. Surface roughness effects on squeeze film poroelastic
772 bearings. Appl. Math. Comput. 174, 1181-1195.
- 773 Chen, T., Buckley, M., Cohen, I., Bonassar, L., Awad, H.A., 2012. Insights into interstitial flow,
774 shear stress, and mass transport effects on ECM heterogeneity in bioreactor-cultivated
775 engineered cartilage hydrogels. Biomech. Model. Mechanobiol. 11, 689-702.
- 776 De Santis, R., Gloria, A., Viglione, S., Maietta, S., Nappi, F., Ambrosio, L., Ronca, D., 2018.
777 3D laser scanning in conjunction with surface texturing to evaluate shift and reduction
778 of the tibiofemoral contact area after meniscectomy. J. Mech. Behav. Biomed. Mater.
779 88, 41-47.
- 780 Fam, H., Bryant, J.T., Kontopoulou, M., 2007. Rheological properties of synovial fluids.
781 Biorheology. 44, 59-74.
- 782 Graham, B.T., Moore, A.C., Burris, D.L., Price, C., 2017. Sliding enhances fluid and solute
783 transport into buried articular cartilage contacts. Osteoarthr. Cartilage 25, 2100-2107.
- 784 Graindorge, S., Ferrandez, W., Ingham, E., Jin, Z., Twigg, P., Fisher, J., 2006. The role of the
785 surface amorphous layer of articular cartilage in joint lubrication. Proc. Inst. Mech. Eng.
786 H. 220, 597-607.
- 787 Greene, G.W., Olszewska, A., Osterberg, M., Zhu, H., Horn, R., 2014. A cartilage-inspired
788 lubrication system. Soft Matter 10, 374-382.
- 789 Hu, Y.Z., Tonder, K., 1992. Simulation of 3-D Random Rough-Surface by 2-D Digital-Filter
790 and Fourier-Analysis. Int. J. Mach. Tool. Manu. 32, 83-90.
- 791 Lai, W.M., Kuei, S.C., Mow, V.C., 1978. Rheological Equations for Synovial-Fluids. J. Biomech.
792 Eng. 100, 169-186.
- 793 Lee, S.S., Duong, C.T., Park, S.H., Cho, Y., Park, S., Park, S., 2013. Frictional response of
794 normal and osteoarthritic articular cartilage in human femoral head. Proc. Inst. Mech.
795 Eng. H 227, 129-137.
- 796 Longmore, R.B., GARDNER, D.L., 1975. Development with age of human articular cartilage
797 surface structure. A survey by interference microscopy of the lateral femoral condyle.
798 Ann. Rheum. Dis. 34, 26-37.

- 799 Marzo, J.M., Gurske-DePerio, J., 2009. Effects of medial meniscus posterior horn avulsion
800 and repair on tibiofemoral contact area and peak contact pressure with clinical
801 implication. *Am. J. Sports. Med.* 37(1), 124-129.
- 802 McCutchen, C.W., 1959. Mechanism of Animal Joints: Sponge-hydrostatic and Weeping
803 Bearings. *Nature.* 184, 1284.
- 804 McCutchen, C.W., 1962. The frictional properties of animal joint. *Wear.* 5, 1-17.
- 805 Merkher, Y., Sivan, S., Maroudas, A., Haiperin, G., Yosef, A., 2006. A rational human joint
806 friction test using a human cartilage-on-cartilage arrangement. *Tribol. Lett.* 22(1), 29-
807 36.
- 808 Miramini, S., Smith, D.W., Zhang, L.H., Gardiner, B.S., 2017. The spatio-temporal mechanical
809 environment of healthy and injured human cartilage during sustained activity and its
810 role in cartilage damage. *J. Mech. Behav. Biomed.* 74, 1-10.
- 811 Moghadam, M.N., Abdel-Sayed, P., Camine, V.M., Pioletti, D.P., 2015. Impact of synovial fluid
812 flow on temperature regulation in knee cartilage. *J. Biomech.* 48, 370-374.
- 813 Moore, A.C., Burris, D.L., 2017. Tribological rehydration of cartilage and its potential role in
814 preserving joint health. *Osteoarthr. Cartilage* 25, 99-107.
- 815 Mow, V.C., Ateshian, G.A., Spilker, R.L., 1993. Biomechanics of diarthrodial joints: a review
816 of twenty years of progress. *J. Biomech. Eng.* 115, 460-467.
- 817 Myant, C., Cann, P., 2013. In contact observation of model synovial fluid lubricating
818 mechanisms. *Tribol. Int.* 63, 97-104.
- 819 Neu, C.P., Komvopoulos, K., Reddi, A.H., 2008. The interface of functional biotribology and
820 regenerative medicine in synovial joints. *Tissue Eng. Part B Rev.* 14(3), 235-247.
- 821 Rushfeldt, P.D., Mann, R.W., Harris, W.H., 1981. Improved techniques for measuring in vitro
822 the geometry and pressure distribution in the human acetabulum. II Instrumented
823 endoprosthesis measurement of articular surface pressure distribution. *J. Biomech.* 14,
824 315-323.
- 825 Schurz, J., Ribitsch, V., 1987. Rheology of Synovial-Fluid. *Biorheology.* 24, 385-399.
- 826 Smyth, P.A., Rifkin, R.E., Jackson, R.L., Hanson, R.R., 2012. A Surface Roughness
827 Comparison of Cartilage in Different Types of Synovial Joints. *J. Biomech. Eng.* 134,
828 021006. DOI: 10.1115/1.4005934.
- 829 Shekhawat, V.K., Laurent, M.P., Muehleman, C., Wimmer, M.A., 2009. Surface topography of
830 viable articular cartilage measured with scanning white light interferometry.
831 *Osteoarthritis. Cartilage* 17, 1197-1203.
- 832 Sokoloff, J.B., 2012. Theory of the effects of surface roughness on fluid lubrication of
833 hydrogels. *Soft Matter* 8, 8164-8170.
- 834 Walker, P.S., Dowson, D., Longfield, M.D., Wright, V., 1968. Boosted Lubrication in Synovial
835 Joints by Fluid Entrapment and Enrichment. *Ann. Rheum. Dis.* 27, 512-520.
- 836 Walker, P.S., Dowson, D., Longfield, M.D., Wright, V., 1969. Lubrication of human joints. *Ann.*
837 *Rheum. Dis.* 28, 194.
- 838 Wu, J.J., 2000. Simulation of rough surfaces with FFT. *Tribol. Int.* 33, 47-58.
- 839 Wu, Y.B., Ferguson, S.J., 2017. The influence of cartilage surface topography on fluid flow in
840 the intra-articular gap. *Comput. Methods Biomech.* 20, 250-259.

841 Zhang, L.H., Miramini, S., Smith, D.W., Gardiner, B.S., Grodzinsky, A.J., 2015. Time Evolution
842 of Deformation in a Human Cartilage Under Cyclic Loading. *Ann. Biomed. Eng.* 43,
843 1166-1177.

844